Applied Physics B (2023) 129:52
https://doi.org/10.1007/s00340-023-07993-1

**Applied Physics B**
**Lasers and Optics**

RESEARCH


# Holographic ultraviolet nanosecond laser processing using adaptive optics

**Satoshi Hasegawa[1] · Mizuki Kato[1] · Yoshio Hayasaki[1]**

Received: 6 October 2022 / Accepted: 22 February 2023


**Abstract**
Fabrication of a through hole in a polyimide film (PI) was demonstrated by holographic ultraviolet (UV) nanosecond laser processing with a computer-generated hologram displayed on a phase-only spatial light modulator (SLM). The UV laser was directly modulated into a Bessel beam by a diffractive axicon displayed on the SLM. The direct modulation contributed to improved light-utilization efficiency of the UV laser and a simplified optical setup compared to the conventional method based on a combination of an SLM and harmonic generation using a nonlinear optical crystal. The Bessel beam reduced the number of pulse shots required for through-hole fabrication to 1/5 compared to the Gaussian beam near the ablation threshold energy of the PI film. Furthermore, adaptive optics was implemented in holographic laser processing to compensate for aberrations in the optical setup. The aberration was reduced to 1/5 compared with before the compensation. The proposed method is suitable for improving the throughput and accuracy of drilling, cutting, and additive manufacturing using UV lasers with industrial requirements.

**Keywords** UV laser processing · Computer-generated hologram · Spatial light modulator · Adaptive optics

## 1 Introduction

Polyimide (PI) films have been widely used in flexible electronics as substrate materials due to their superior physical properties [1], such as low dielectric constant, excellent thermal stability, and high mechanical strength. Various methods have been developed to process PI films, including chemical etching [2], plasma discharge [3], and laser irradiation [4]. In particular, the laser irradiation method has valuable advantages in terms of relatively low-cost equipment, environmental friendliness due to the dry process, and maskless patterning. In laser processing of PI films, ultraviolet (UV) lasers have been commonly used [4], because PI films exhibit strong absorption in the UV wavelength region, and UV lasers have specific advantages for processing, including high spatial resolution due to the short wavelength and a minimal heat-affected zone derived from the non-thermal process involving the high-energy photons [5]. The demand for miniaturization and high-speed operation of electronic devices has encouraged high-density processing of PI films. As a result, the throughput of UV laser processing has become important, because the throughput is directly related to the device manufacturing cost. Throughput improvements have been continuously sought using high-speed motorized stages and galvanometer mirrors in combination with high-repetition-rate pulsed lasers.

Another approach to increase the throughput by employing holographic laser processing using a computer-generated hologram (CGH) displayed on a spatial light modulator (SLM) has also been developed [6–8]. Studies on beam shaping [9, 10], multi-beam generation [11–13], and pulse shaping [14–16] using an SLM in the UV wavelength region have been reported and applied to a wide range of areas including optical lithography [9], laser microsurgery of cells [11], and laser processing of polymer materials [12, 13]. In these studies, a liquid crystal SLM (LC-SLM) was often used [11–14] because of its high light-utilization efficiency due to a phase-only modulation ability and a large number of pixels; for instance, recently, LC-SLMs with 4k×2k pixels have become commercially available. Since liquid crystal materials have issues with durability in the UV wavelength range, especially ultrashort pulsed laser light, a method based on converting near-infrared laser light into UV

✉ Satoshi Hasegawa
hasegawa_s@cc.utsunomiya-u.ac.jp

[1] Center for Optical Research and Education, Utsunomiya University, 7-1-2 Yoto, Utsunomiya 321-8585, Japan

Published online: 18 March 2023

laser light using harmonic generation by a nonlinear optical crystal placed after the LC-SLM was proposed to avoid optical damage to the LC-SLM due to the UV laser irradiation [12–14]. On the other hand, micro-electro-mechanical system (MEMS)–SLMs [15] with high reflectivity in the UV range and fused-silica acousto-optical modulators (AOMs) [16] with high transmittance were also used instead of LC-SLMs. Recently, SLMs that are relatively tolerant to UV laser light at wavelengths near 350 nm have become commercially available [17].

In this paper, we demonstrated, for the first time, beam shaping of UV nanosecond laser light by direct modulation using an LC-SLM only (without a nonlinear optical crystal) and applied it to laser processing of PI films. In an experiment, a through hole was processed on a PI film using a Bessel beam generated by a diffractive axicon displayed on the LC-SLM. Furthermore, adaptive optics was also implemented in holographic laser processing to compensate for optical aberrations mainly derived from surface distortion of the LC-SLM. In the UV wavelength range, the influence of the aberrations on the quality of the focused beam is more sensitive than that in the visible wavelength range. The direct modulation contributed to improving the light-utilization efficiency of the UV laser light because the reflectivity of the LC-SLM for the UV wavelength was more than 86%, which is larger than the typical conversion efficiency ($\eta = \sim 50\%$) of second harmonic generation using a $\beta$-barium borate (BBO) nonlinear optical crystal in combination with the LC-SLM. In addition, the proposed method simplified the optical system and eliminated the need for fine alignment associated with the phase matching of the nonlinear optical crystal. Furthermore, vector beams in the UV wavelength region can be directly generated by the LC-SLM, because a polarization-dependent nonlinear optical crystal is not used. Vector beams have recently attracted attention due to the novel properties they offer, such as focusing into a spot size beyond the diffraction limit owing to the longitudinal vector component of a radially polarized beam focused by a high-numerical-aperture objective lens [18] and fabrication of periodic nanostructures with femtosecond lasers [19].

In the Principle section, the design method of a diffractive axicon for generating a Bessel beam and adaptive optics based on Zernike polynomials are described. In the Experimental setup section, the optical setup used for the experiments is shown. In the Experimental results section, the diameter of the through hole versus the number of pulse shots was compared in processing using a Bessel beam and a Gaussian beam in the UV region. The Bessel beam improved the throughput of processing because its depth of focus was larger compared with that of the Gaussian beam. Finally, adaptive optics compensated for the deformation of the focused UV laser beam derived from the aberrations in the optical setup and improved the accuracy of laser processing. In the Conclusion section, we summarize our paper.

## 2 Principle

### 2.1 Design of diffractive axicon for generating Bessel beam

The phase distribution $\phi$ and the complex amplitude $u$ of the CGH on the SLM are expressed by

$$\phi(r) = \mathrm{mod}\left(\frac{-kr^{\alpha}}{2f}, 2\pi\right), \tag{1}$$

$$u(r) = a(r)\exp i[\phi(r)], \tag{2}$$

respectively, where $r = (x^2 + y^2)^{1/2}$ is the position in a cylindrical coordinate system, mod is the remainder (modulo) operator, $k = 2\pi/\lambda$ is the wave number, $f$ is the focal length of the CGH, $\alpha$ is a constant and $a$ is the amplitude distribution (Gaussian) of a beam illuminating the CGH. When $\alpha$ is set to 1 or 2, the diffractive axicon or lens is selectively obtained, respectively. Figure 1a, b shows the phase distribution of the diffractive lens and axicon with $f = 10000$ and 2000 mm, respectively, and their axial and lateral intensity distributions versus the distance on the optical ($z$) axis in a simulation. The grayscale of the phase distribution represents the phase range from 0 to $2\pi$. A lens with a focal length of $f_F$ was placed behind the CGH to perform the optical Fourier transform. The distance $z$ is defined as the distance from the Fourier plane ($z = 0$) of the CGH. The inserted intensity profile was normalized by the maximum value in the profile. Based on scalar diffraction theory to propagate the complex amplitude [20, 21], the intensity distribution $I$ of the CGH reconstruction on an arbitrary $z$ plane is expressed with a lens term $\phi_{\mathrm{L}}$ as

$$I(\rho, z) = |f[u_{\mathrm{L}}(r, z)]|^2, \tag{3}$$

$$u_{\mathrm{L}}(r, z) = a(r)\exp i[\phi(r) + \phi_{\mathrm{L}}(r, z)], \tag{4}$$

$$\phi_{\mathrm{L}}(r, z) = -\frac{\pi z r^2}{\lambda f_F^2}, \tag{5}$$

where $\rho = (v_x^2 + v_y^2)^{1/2}$ is the position in the Fourier plane, and $f$ denotes a Fourier transform. In the simulation, the full width at half maximum (FWHM) of the axial intensity profile of the diffractive axicon (Fig. 1b) was 3.5 times larger than that of the diffractive lens (Fig. 1a). The rightmost figure shows the lateral intensity image of the reconstruction at the $z$ position indicated by a white dashed line in the axial intensity distribution. The Bessel beam had a concentric

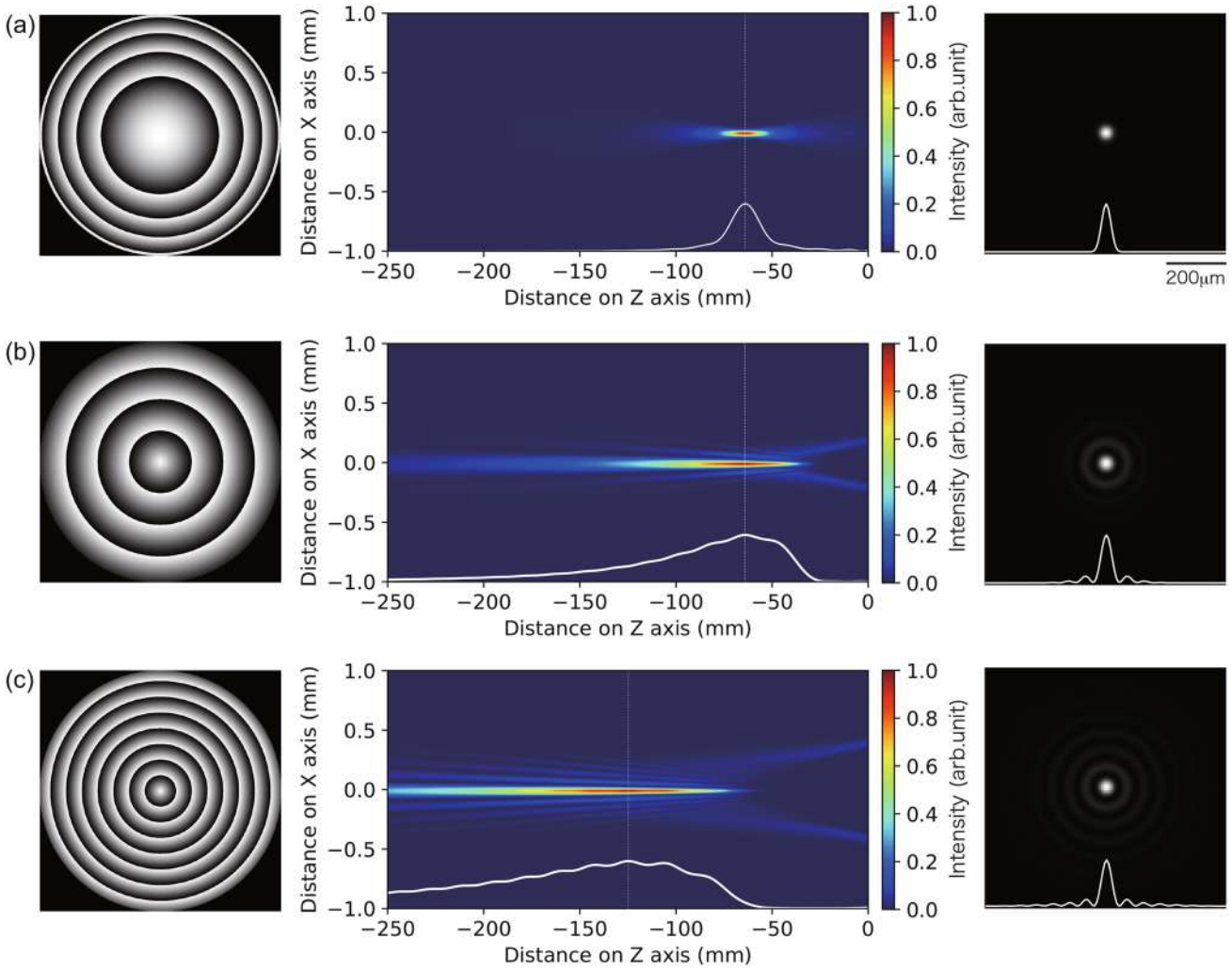


**Fig. 1** Phase distributions and axial and lateral intensity distributions versus the distance on the $z$-axis in the case of **a** diffractive lens with $f$ = 10000 mm and the diffractive axicon with **b** $f$ = 2000 and **c** 1000 mm

sidelobe. Figure 1c shows the phase distribution of the diffractive axicon with $f$ = 1000 mm and its axial and lateral intensity distributions. By adjusting $f$, the depth of focus of the Bessel beam was arbitrarily controlled. In this experiment, a diffractive lens with $f$ = 10000 mm (Fig. 1a) and a diffractive axicon with $f$ = 2000 mm (Fig. 1b) were used.

## 2.2 Aberration compensation using Zernike polynomials

In an optical system using an objective lens (OL), the adaptive optics corresponds to compensating for the distortion of the wavefront on the pupil plane. The aberration $w$ is approximated based on Zernike polynomials [22] and is given by

$$w(r,\theta) = \sum_{i=1}^{\infty} c_i Z_i(r,\theta), \tag{6}$$

where $r$ and $\theta$ are the radius and argument in polar coordinates, respectively, $i$ indicates Zernike modes, and $c$ and $Z$ are Zernike coefficients and Zernike polynomials, respectively. Figure 2a, b shows the mathematical expression for each Zernike mode and its phase distribution, where $n$ and $m$ are radial order and azimuthal frequency, respectively. In this experiment, $c$ is measured by a Shack–Hartmann wavefront sensor [23] placed at the pupil plane of the OL. A computer calculates the phase distribution $w^*$ (conjugate phase of $w$) based on the obtained $c$ and displays $w^*$ on the SLM to compensate for the aberrations.

(a)

| i | n | m | $Z_i(r,\theta)$ |
|---|---|---|---|
| 1 | 0 | 0 | 1 |
| 2 | 1 | 1 | $2r\cos\theta$ |
| 3 | | -1 | $2r\sin\theta$ |
| 4 | 2 | 0 | $\sqrt{3}(2r^2-1)$ |
| 5 | | 2 | $\sqrt{6}r^2\cos(2\theta)$ |
| 6 | | -2 | $\sqrt{6}r^2\sin(2\theta)$ |
| 7 | 3 | 1 | $\sqrt{8}(3r^3-2r)\cos\theta$ |
| 8 | | -1 | $\sqrt{8}(3r^3-2r)\sin\theta$ |
| 9 | | 3 | $\sqrt{8}r^3\cos(3\theta)$ |
| 10 | | -3 | $\sqrt{8}r^3\sin(3\theta)$ |
| 11 | 4 | 0 | $\sqrt{5}(6r^4-6r^2+1)$ |

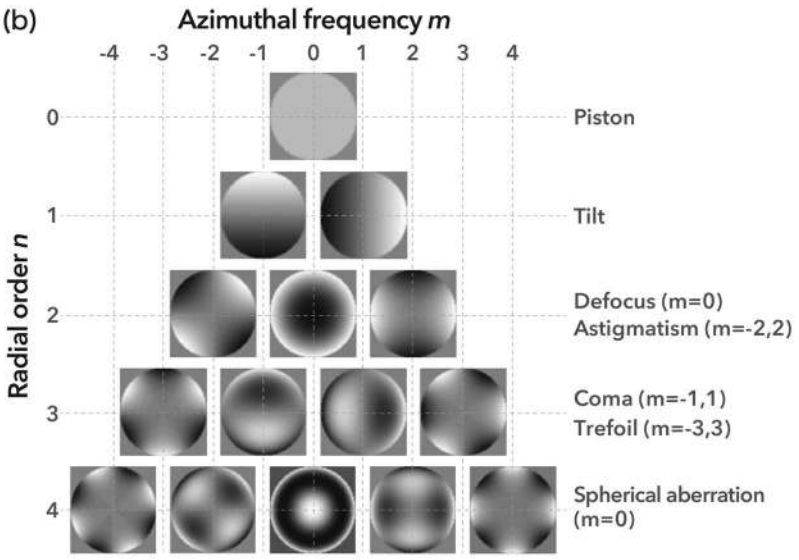


**Fig. 2** **a** Mathematical expression for each Zernike mode and **b** its phase distribution

## 3 Experimental setup

Figure 3 shows the experimental setup. A nanosecond laser pulse emitted from a Q-switched Nd:YAG laser with third-harmonic generation (COHERENT, AVIA 355-7HP) had a wavelength of 355 nm, a pulse duration of 35 ns, and a repetition frequency up to 300 kHz (set to 10 kHz in the experiment), and was radiated onto a liquid-crystal-on-silicon SLM (LCoS-SLM; Santec, SLM-150) through a neutral density (ND) filter to control the pulse energy, a polarizer (POL) to obtain the p-polarization, and 3× beam expanding optics (BE). The phase distributions of the designed diffractive lens (Fig. 1a) and diffractive axion (Fig. 1b) were displayed on the SLM to generate Gaussian and Bessel beams. The pulse was diffracted by the CGH displayed on the LCoS-SLM and was introduced to laser processing optics composed of the OL (Chuo seiki, OB-10, ×10, NA = 0.25, $f$ = 15.5 mm) using 4f imaging optics (L1 with $f$ = 800 mm and L2 with $f$ = 400 mm). The reflectance of the SLM for the UV wavelength was more than 86% in the specification. The wavefront at the pupil plane of the OL was measured by a Shack–Hartmann wavefront sensor (WFS; Thorlabs, WFS150C) when no CGH was displayed on the LCoS-SLM. The phase conjugation of the wavefront was calculated by a computer and was displayed on the SLM to compensate for the aberration. A halogen lamp, a dichroic mirror (DM), and a complementary metal-oxide-semiconductor (CMOS) image sensor (IS) were used to observe the processed structure. A polyimide film with a thickness of 12 $\mu$m was mounted on a three-axis linear micro-stage as a sample. The processed structure was analyzed in detail using a scanning electron microscope (SEM) (Hitachi, S-4500) and a laser confocal microscope (LCM) (Olympus, OLS4000).

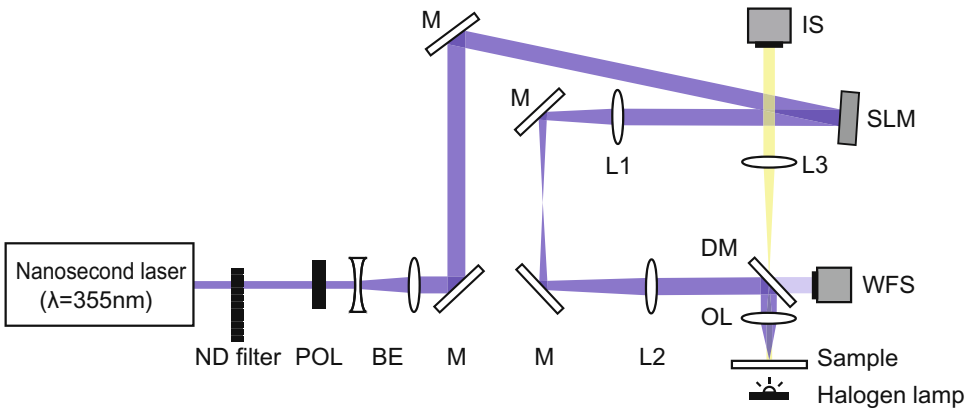


**Fig. 3** Experimental setup. *POL* polarizer, *BE* beam expander, *M* mirror, *L* lens, *DM* dichroic mirror, *OL* objective lens, *WFS* wavefront sensor, *IS* image sensor

## 4 Experimental results

### 4.1 Processing properties of PI film processed by UV Bessel beam

The processing properties of the PI film processed by UV laser light were investigated. Figure 4 shows the diameter of the structure processed on the surface of the PI film versus the pulse energy of the UV laser. In processing, the number of pulse shots was set to a single shot and the focusing position was set to 6 $\mu$m inside the PI film. The gray and black lines indicate the result obtained using the diffractive lens (Gaussian beam) and axicon (Bessel beam), respectively. The inset of the graph shows a microscope image obtained by the LCM. The diameter was defined as the maximum distance between the zero-crossing positions in the depth profile of the structure obtained by the LCM, as shown in the inset. At the pulse energy near the ablation threshold, the side lobe of the Bessel beam did not contribute to processing. On the other hand, at the pulse energy above 200 nJ, the influence of the sidelobe was observed. As a result, the ablation threshold of the PI film when using the Gaussian beam was about half that of the Bessel beam. The diameter of the structure processed with the Bessel beam was 0.47 times smaller than that with the Gaussian beam at the pulse energy of 61 nJ. The increase in ablation threshold and the reduction in diameter are attributed to the decrease in fluence due to the extended depth of focus obtained with the use of the Bessel beam.

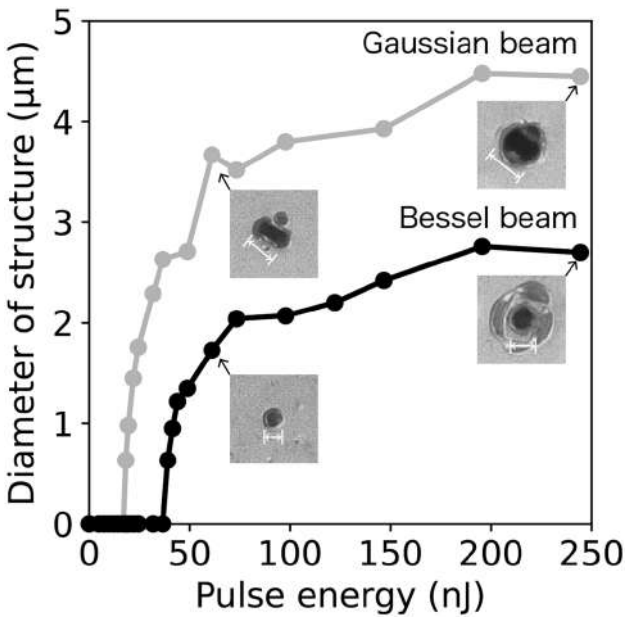


**Fig. 4** Diameter of the structure processed on the surface of the PI film versus the pulse energy of the UV laser. The gray and black lines indicate the results obtained using the Gaussian beam and Bessel beam, respectively

### 4.2 Through-hole fabrication using UV Bessel beam

Through-hole fabrication was performed using the Gaussian and Bessel beams. The minimum pulse energy required to fabricate the through hole was the same (40 nJ) for both the Gaussian and Bessel beams. On the other hand, the number of pulse shots required to process the through hole was different for the two beams: 5000 and 1000 pulses, respectively, when the pulse energy was set to 40 nJ. Figure 5a, b shows the LCM image of the structure processed on the front and rear surface of the PI film in the through-hole fabrication using the Gaussian and Bessel beams, respectively, when the number of pulse shots was varied. The pulse energy was fixed to 159 nJ. In Fig. 5b, the dashed circle means the area of the structure processed by the main lobe of the Bessel beam. Figure 5c shows the diameter of the through hole on the front and rear surface using the Gaussian and Bessel beam versus the number of pulse shots. The gray and black lines indicate the results obtained using the Gaussian and Bessel beams, respectively. In both cases, there was no difference in the change in diameter of the structure processed on the front surface with an increasing number of pulse shots. On the other hand, the diameter of the structure processed on the rear surface with the Bessel beam was larger than that with the Gaussian beam. The diameter ratio between the structures on the front and the rear surfaces was 0.47 and 0.85 in the case of the Gaussian and Bessel beams, respectively, when the number of pulse shots was 10 thousand. As a result, the Bessel beam performed the through-hole fabrication more efficiently.

### 4.3 Aberration compensation using adaptive optics

In the processing of the PI film, the structure was distorted rather than ideally circular in the high pulse energy region. This distortion is due to optical aberrations caused by the misalignment of the optical setup and the non-flatness of the SLM. In this experiment, aberration compensation was applied to UV laser processing to improve the accuracy. Figure 6a shows the Zernike coefficient of the wavefront at the pupil plane of the OL, obtained by the wavefront sensor. The gray and black bars indicate the Zernike coefficient before and after the compensation, respectively. In the compensation, the piston, tilt and defocus components corresponding to Zernike mode numbers 1, 2, 3, and 4 were ignored, because they do not affect the distortion of the focused beam. The minimum value of the coefficient was 1 nm, which corresponds to the sensitivity level of the wavefront sensor. As a result, the main aberration was astigmatism, corresponding to Zernike mode numbers 5 and 6, which originated from

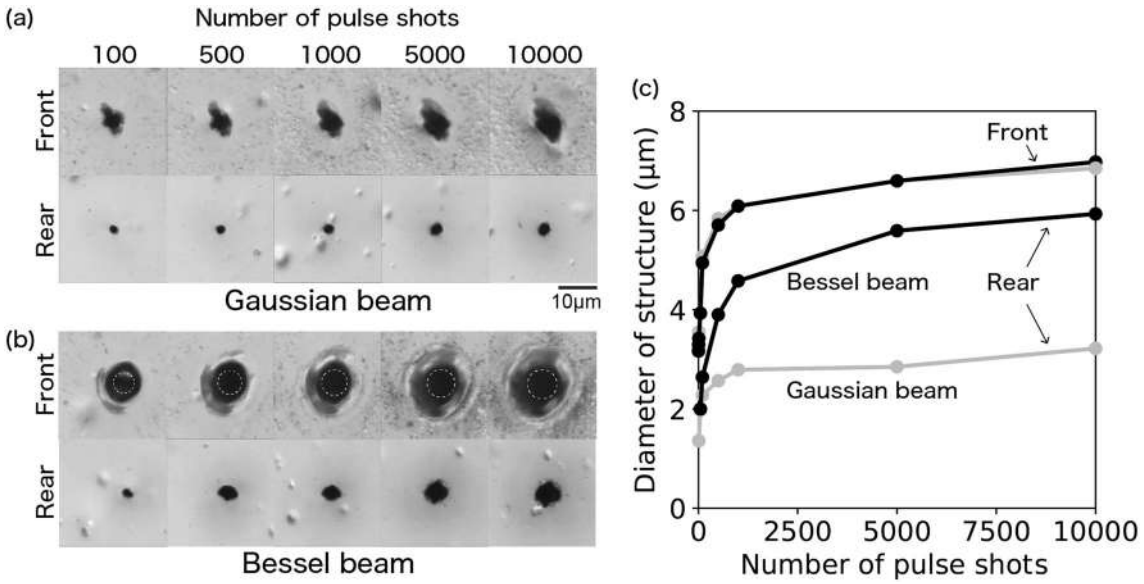


**Fig. 5** LCM images of the structures processed on the front and rear surfaces of the PI film using **a** Gaussian and **b** Bessel beam when the number of pulse shots was varied. **c** Diameter of the structure versus the number of pulse shots

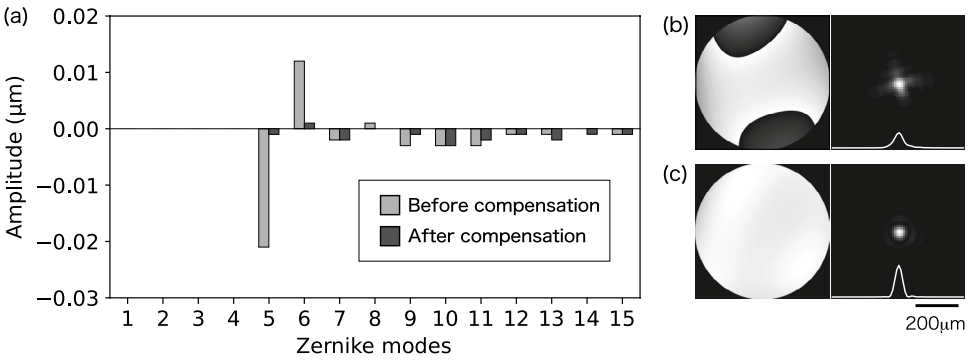


**Fig. 6** **a** Zernike coefficient corresponding to the wavefront at the pupil of the objective lens. The wavefront on the pupil plane and corresponding focused beam **b** without and **c** with the aberration compensation in the simulation

the non-flatness of the LC-SLM. In the case without and with the compensation, the root mean square (RMS) of the Zernike coefficient was 7.5 and 1.6 nm, respectively. The compensation reduced the aberration to about 1/5. Figure 6b, c shows the wavefront obtained using the Zernike coefficient and the intensity distribution of the focused beam in the case without and with the compensation in the computer simulation, respectively. Both intensity profiles were normalized by the peak intensity in the case with the compensation. The peak intensity with the compensation was 2.1 times larger than that without the compensation.

## 4.4 UV laser processing with adaptive optics

The effect of wavefront compensation was verified through UV laser processing of the PI film. Figure 7a, b shows the LCM image of the processed structure versus the pulse energy without and with the aberration compensation,

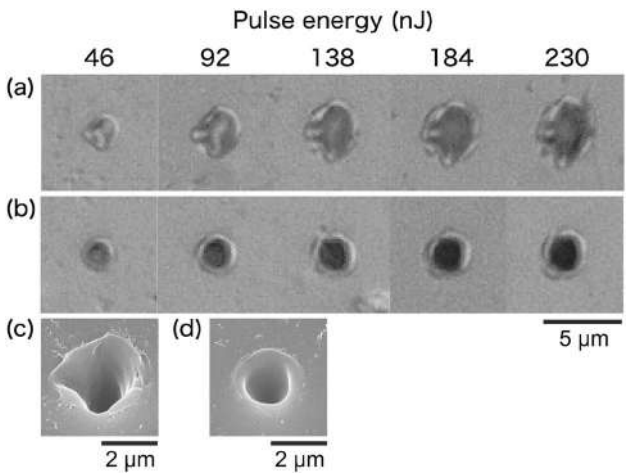


**Fig. 7** LCM image of processed structure versus pulse energy **a** without and **b** with the aberration compensation. SEM image of the structure **c** without and **d** with the compensation when the pulse energy was 138 nJ

respectively. In the case without the compensation, the diffractive lens (Fig. 1a) was used. In the case with the compensation, the diffractive lens superimposed on the phase conjugation of the wavefront (Fig. 6b) was used. The number of pulse shots was set to a single shot, and the focusing position was set to the surface of the PI film. Figure 7c, d shows the SEM image of the structure when the pulse energy was set to 138 nJ in the cases without and with the compensation, respectively.

Figure 8a shows the diameter of the processed structure versus the pulse energy. In the graph, gray and black lines indicate the result without and with the aberration compensation, respectively. The inset shows the SEM image of the processed structure at each pulse energy. In the case with the compensation, the threshold energy required to process the structure was 0.61 times smaller than that in the case without the compensation. Furthermore, the minimum diameter of the structure was 797 nm, which was smaller than the diffraction limited-beam size of 1.7 $\mu$m. The reduction in ablation threshold and the reduction in the structure diameter were due to the improvement of the quality of the focused beam by the aberration compensation.

Figure 8b shows the roundness of the processed structure versus the pulse energy. The roundness was evaluated based on the minimum circumscribed circle (MCC) method, as shown on the right side of the figure. The MCC method is the radial difference between the smallest circumscribed circle $R_{max}$ surrounding the object and the smallest concentric inscribed circle $R_{min}$. In this experiment, the roundness was defined as the ratio between $R_{max}$ and $R_{min}$; that is, a ratio of 1 means an ideal circular shape. As a result, there was

no difference in the roundness of the structure near the ablation threshold (less than 40 nJ) between the two cases. The reason for this is due to a threshold effect [24] in which only the central part of the beam contributes to the ablation by choosing the peak laser intensity slightly above the ablation threshold. On the other hand, there was a large difference in roundness between the two cases in the high pulse energy region because the distortion of the intensity distribution around the peak intensity contributed to the formation of the structure. In the case with the compensation, the roundness was slightly larger than 1. The reason for this may be due to a small deviation between the transverse and longitudinal Gaussian profiles of the focused beam, which originated from the characteristics of the laser source.

Figure 9a, b shows LCM images of the structures processed by multi-spot beams without and with the aberration compensation, respectively. In the case with the compensation, a CGH that generated 4 parallel beams superimposed on the phase conjugation of the wavefront (Fig. 6b) was used. The number of pulse shots and the pulse energy were set to a single shot and 280 nJ, respectively, in both cases. The adaptive optics improved the accuracy of holographic UV laser processing.

## 5 Conclusion

The through-hole fabrication of the PI film was demonstrated by holographic UV nanosecond laser processing with the CGH displayed on the phase-only LC-SLM. The UV laser was directly modulated into a Bessel beam by the LC-SLM. The direct modulation contributed to improving the light-utilization efficiency of the UV laser and simplifying

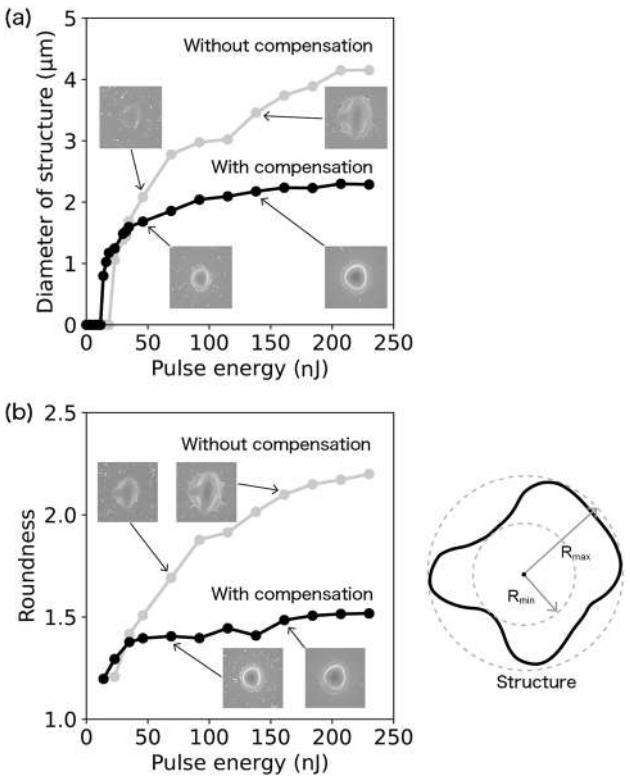


**Fig. 8** **a** Diameter and **b** roundness of processed structure versus the pulse energy without and with the aberration compensation

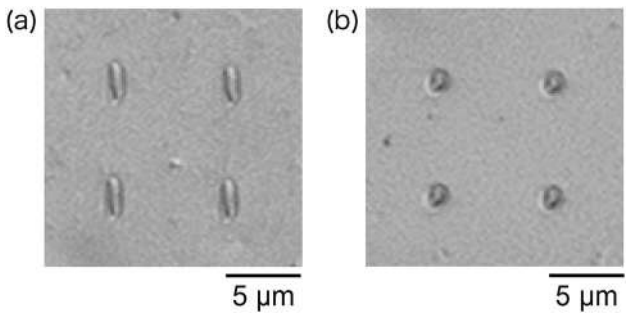


**Fig. 9** LCM image of the structure processed by the multi-spot beams **a** without and **b** with the aberration compensation

the optical setup. In the through-hole fabrication, the Bessel beam reduced the number of pulse shots required to process the through hole and increased the diameter of the structure on the rear surface of the PI film compared to the Gaussian beam. Furthermore, adaptive optics was implemented in holographic laser processing to compensate for the aberrations in the optical setup. The main aberration measured by the wavefront sensor was astigmatism, which originated from the non-flatness of the LC-SLM. The aberration compensation reduced the RMS of the Zernike coefficient to about 1/5 compared with before the compensation. Finally, the effect of the aberration compensation was verified through UV laser processing of the PI film. The aberration compensation improved the quality of the focused beam and contributed to a lower ablation threshold, smaller structure diameter, and improved roundness of the structure. The proposed method is useful for improving the throughput and accuracy of drilling, cutting, and additive manufacturing using UV lasers. In addition, these applications will further accelerate the development of SLMs that are tolerant to UV wavelengths.

**Funding** This work was supported by JSPS KAKENHI Grant Number JP22K03855 and the Council for Science, Technology and Innovation (CSTI), Cross-ministerial Strategic Innovation Promotion Program (SIP), "Photonics and Quantum Technology for Society 5.0" (Funding agency: QST).

## Declarations

**Conflict of interest** The authors declare no conflicts of interest.

## References

1. P.M. Hergenrother, The use, design, synthesis, and properties of high performance/high temperature polymers: an overview. High Perform. Polym. **15**(1), 3–45 (2003)
2. S.-M. Lian, K.-M. Chen, R.-J. Lee, J.-P. Pan, A. Hung, Chemical etching of polyimide film. J. Appl. Polym. Sci. **58**(9), 1577–1584 (1995)
3. B. Lamontagne, A. Wrobel, G. Jalbert, M. Wertheimer, Large-area microwave plasma etching of polyimide. J. Phys. D Appl. Phys. **20**(7), 844 (1987)
4. R. Srinivasan, B. Braren, R. Dreyfus, Ultraviolet laser ablation of polyimide films. J. Appl. Phys. **61**(1), 372–376 (1987)
5. Q. Lou, T. Li, Microprocessing by UV laser. Proc. SPIE **4915**, 1–12 (2002)
6. Y. Hayasaki, T. Sugimoto, A. Takita, N. Nishida, Variable holographic femtosecond laser processing by use of a spatial light modulator. Appl. Phys. Lett. **87**(3), 031101 (2005)
7. N. Sanner, N. Huot, E. Audouard, C. Larat, J.-P. Huignard, B. Loiseaux, Programmable focal spot shaping of amplified femtosecond laser pulses. Opt. Lett. **30**(12), 1479–1481 (2005)
8. S. Hasegawa, Y. Hayasaki, N. Nishida, Holographic femtosecond laser processing with multiplexed phase fresnel lenses. Opt. Lett. **31**(11), 1705–1707 (2006)
9. C. Chatwin, M. Farsari, S. Huang, M. Heywood, P. Birch, R. Young, J. Richardson, UV microstereolithography system that uses spatial light modulator technology. Appl. Opt. **37**(32), 7514–7522 (1998)
10. S. Li, Y. Wang, Z. Lu, L. Ding, C. Cui, Y. Chen, D. Pengyuan, D. Ba, Z. Zheng, H. Yuan, L. Shi, Z. Bai, Z. Liu, C. Zhu, Y. Dong, L. Zhou, Spatial beam shaping for high-power frequency tripling lasers based on a liquid crystal spatial light modulator. Opt. Commun. **367**(15), 181–185 (2016)
11. A.K. Jayasinghe, J. Rohner, M.S. Hutson, Holographic UV laser microsurgery. Biomed. Opt. Express **2**(9), 2590–2599 (2011)
12. D. Liu, W. Perrie, Z. Kuang, P. Scully, A. Baum, S. Liang, S. Edwardson, E. Fearon, G. Dearden, K. Watkins, Multi-beam second-harmonic generation in beta barium borate with a spatial light modulator and application to internal structuring in poly (methyl methacrylate). Appl. Phys. B **107**(3), 795–801 (2012)
13. L. Ye, W. Perrie, O. Allegre, Y. Jin, Z. Kuang, P. Scully, E. Fearon, D. Eckford, S. Edwardson, G. Dearden, NUV femtosecond laser inscription of volume bragg gratings in poly (methyl) methacrylate with linear and circular polarizations. Laser Phys. **23**(12), 126004 (2013)
14. M. Hacker, T. Feurer, R. Sauerbrey, T. Lucza, G. Szabo, Programmable femtosecond laser pulses in the ultraviolet. J. Opt. Soc. Am. B **18**(6), 866–871 (2001)
15. M. Hacker, G. Stobrawa, R. Sauerbrey, T. Buckup, M. Motzkus, M. Wildenhain, A. Gehner, Micromirror SLM for femtosecond pulse shaping in the ultraviolet. Appl. Phys. B **76**(6), 711–714 (2003)
16. M. Roth, M. Mehendale, A. Bartelt, H. Rabitz, Acousto-optical shaping of ultraviolet femtosecond pulses. Appl. Phys. B **80**(4), 441–444 (2005)
17. Y. Sakurai, M. Nishitateno, M. Ito, K. Takatoh, UV durable LCOS for laser processing. Crystals **11**(9), 1047 (2021)
18. B. Jia, H. Kang, J. Li, M. Gu, Use of radially polarized beams in three-dimensional photonic crystal fabrication with the two-photon polymerization method. Opt. Lett. **34**(13), 1918–1920 (2009)
19. S. Hasegawa, Y. Hayasaki, Holographic femtosecond laser manipulation for advanced material processing. Adv. Opt. Technol. **5**(1), 39–54 (2016)
20. J.E. Curtis, B.A. Koss, D.G. Grier, Dynamic holographic optical tweezers. Opt. Commun. **207**(1–6), 169–175 (2002)
21. R. Di Leonardo, F. Ianni, G. Ruocco, Computer generation of optimal holograms for optical trap arrays. Opt. Express **15**(4), 1913–1922 (2007)
22. J. Wang, D.E. Silva, Wave-front interpretation with Zernike polynomials. Appl. Opt. **19**(9), 1510–1518 (1980)
23. B.C. Platt, R. Shack, History and principles of Shack-Hartmann wavefront sensing. J. Refract. Surg. **17**(5), S573–S577 (2001)
24. F. Korte, J. Serbin, J. Koch, A. Egbert, C. Fallnich, A. Ostendorf, B. Chichkov, Towards nanostructuring with femtosecond laser pulses. Appl. Phys. A **77**(2), 229–235 (2003)